Temperature insensitive mass sensing of mode selected phononic crystal cavity

2015 J. Micromech. Microeng. 25 125027

(http://iopscience.iop.org/0960-1317/25/12/125027)

IOP Publishing Journal of Micromechanics and Microengineering
J. Micromech. Microeng. **25** (2015) 125027 (8pp) doi:10.1088/0960-1317/25/12/125027

Temperature insensitive mass sensing of mode selected phononic crystal cavity

Peng Li[1,2], Feng Li[1], Yongshun Liu[1], Fengfeng Shu[1,2], Junfeng Wu[1] and Yihui Wu[1]

[1] State Key Laboratory of Applied Optics, Changchun Institute of Optics, Fine Mechanics and Physics, Chinese Academy of Sciences, Changchun 130033, People's Republic of China
[2] University of Chinese Academy of Sciences, Beijing 100049, People's Republic of China

E-mail: yihuiwu@ciomp.ac.cn

Received 14 August 2015, revised 28 September 2015
Accepted for publication 12 October 2015
Published 13 November 2015

Abstract

Phononic crystal cavities with high quality (Q) factors are attractive in both signal processing and sensing applications. In this paper, 2D phononic crystal point defect cavities are fabricated on silicon slabs by micro electromechanical system (MEMS) technologies. An electrode design method is proposed to enhance displacements of the point defect modes. Then the method is applied to design MEMS resonators with different port numbers, among which Q factor as high as 21 300 is obtained in air. Multiport resonators with transmission measurements are proved to be advantageous over one-port resonators with impedance measurements in frequency resolution. A temperature insensitive resonant mass sensor is designed based on a two-port resonator. Two defect modes with strong responses in the two-port resonator are combined to compensate environmental temperature interference. The temperature compensation experiment reveals that temperature interference is effectively compensated from mass measurement and the mass sensitivity of the sensor is 5.4 Hz ng^{-1}. The conclusion of mode selection or sensing mechanism will help to design resonators or sensors with high performances.

Keywords: phononic crystal, resonant mode selection, mass sensor, temperature compensation

(Some figures may appear in colour only in the online journal)

1. Introduction

Phononic crystals (PnCs) have drawn wide attention in recent years because they can manipulate acoustic waves efficiently [1–9]. One striking feature of PnCs is that bandgap structure may exist and the wave propagation will be prohibited [1]. The introduction of defects into the otherwise perfect PnCs will lead to vibrations with frequencies within the bandgap localized in the defects, i.e. defect modes [7–9]. The localized defect modes, which have high quality (Q) factors, are promising in both signal processing and sensing applications. Recently, silicon (Si) based 2D linear defect PnC devices [7, 8] and point defect on steel plates [9] have been investigated. In all cases, high Q factors are obtained. However, the better energy confinement by point defects and the compatibility with CMOS processing determine that a study of Si based point defect cavities is still needed.

Although PnCs have been widely investigated, their sensing applications have seldom been explored. Lucklum *et al* first applied PnC cavities to sense liquid sound velocity [10]. Amoudache *et al* further discussed the simultaneous sensing of light and sound velocities of liquids by combining phononic and photonic crystals—phoXonic crystals with defects [11]. PnC cavities usually support several distinct resonant modes. The multimode behavior in sensing applications can help to realize multiple parameter measurement on a single device [12–15]. With their high Q performance and tiny resonant mass, PnC point defects can be good candidates for high Q mass sensors like quartz crystal microbalance (QCM). But compared with QCM, the PnC mass sensor is easily interfered with by ambient temperature drifts, which can seriously distort the measurement of mass sensing. The passive temperature compensation utilizing the opposite temperature sensitivities of the symmetric mode and antisymmetric mode in liquid

has been demonstrated by Lamb-wave sensors [12]. But the same strategy is not applicable to the bulk Si PnC mass sensor, because all defect modes are expected to have similar temperature sensitivities of about -31 ppm°C^{-1} [16]. However, the diverse vibration energy distributions of the defect modes can lead to striking mass sensitivity differences in some parts of the sensor surface [14] and provide another approach to cancel out thermal disturbances. While the multimode characteristic of point defects can help with temperature compensation, it also brings the difficulty of exciting the modes efficiently.

The PnC point defect structures in this paper are actuated by piezoelectric aluminum nitride (AlN) film deposited on top of a Si substrate, and the electrode layout affects mode displacements greatly. As the interdigital electrodes outside the defect [7] that produce plane waves are inefficient for the point excitation, we put the electrode in the cavity and thus can control mode responses more directly. The selective mode excitation of linear defect PnC resonator has been realized by simply shifting the electrode [17], but it still needs further systematic investigations. The concept of modal sensors/actuators was initially proposed in [18], and further developed to control the mode displacements of microplate resonators [19, 20]. Motivated by this concept, and based on the Butterworth–Van Dyke equivalent circuit model for piezoelectric resonators [21, 22], we propose an electrode design method to maximize the displacements of the point defect modes.

In the second part of this paper, we analyze the point defect modes and introduce the fabrication procedure. In the third part, we deduce the mode selection method and apply it to design resonators with different port numbers. In the fourth part, we show the temperature compensation experiments. Finally we discuss the experiment results and make conclusions.

2. Mode analysis and device fabrication

The hexagonal PnC structure is built by etching holes in a 380 μm thick Si slab. In order to maximize the band gap, the distance between the nearest holes a is equal to the slab thickness d [23]. The radius of holes r is 170 μm. A unit cell is shown in figure 1(a) and there is an anticlockwise rotation of the PnC coordinate axes xyz through an angle of 45° about the z' axis of the Si coordinate system $x'y'z'$. Using the finite element method (FEM) software COMSOL and applying Bloch boundary conditions for periodic systems, the band structure of the PnC in the reduced Brillouin zone (figure 1(b)) is calculated. The values of the stiffness tensor for Si used are $C_{11} = 166$ GPa, $C_{12} = 64$ GPa, $C_{44} = 80$ GPa and the density is 2330 kg m^{-3}, taken from COMSOL. The band structure reveals a complete band gap extending from 4.3 to 6.0 MHz, as shown in figure 1(c).

The investigated point defect is formed by simply removing one unit cell. Using the supercell method and the FEM, six defect modes are obtained whose mode shapes are presented in figure 2. It should be noted that the 45° rotation angle in figure 1(a) is selected after calculations to ensure that the defect modes are away from the lower bound of the band gap, for better energy confinement. The defect modes exhibit distinct vibration types, including torsion, extension, flexure or a combination, which is favorable in meeting various application requirements. The resonant properties of the modes can be modulated by adjusting the defect structure. In the passive temperature compensation utilizing dual modes, the normalized relative resonant frequency shifts of both modes, i.e. $\Delta f_1/f_1$ and $\Delta f_2/f_2$, can be approximated as the linear function of mass attachment Δm and temperature drift ΔT, that is,

$$\begin{bmatrix} \Delta f_1/f_1 \\ \Delta f_2/f_2 \end{bmatrix} = \begin{bmatrix} \alpha_1/f_1 & \beta_1 \\ \alpha_2/f_2 & \beta_2 \end{bmatrix} = \begin{bmatrix} \Delta m \\ \Delta T \end{bmatrix}, \tag{1}$$

where α_1 and α_2 are mass sensitivities expressed in Hz ng^{-1}, and β_1 and β_2 are temperature sensitivities expressed in ppm °C^{-1}. Since β_1 and β_2 are expected to be about -31 ppm°C^{-1}, we turn to find the specific sensing surface where there is a huge difference in α_1 and α_2. Based on perturbation theory [24], the mass sensitivity of the point cavity on surface A can be evaluated as

$$\alpha = \frac{\Delta f}{\Delta m} = -\frac{f_0 \int_A U^2 \mathrm{d}A}{2A_0 \int_V \rho U^2 \mathrm{d}V}, \tag{2}$$

where Δm is the loaded mass, A_0 is the area of surface A, f_0 is the mode frequency, U is the amplitude of total displacement field, ρ is the cavity density (Si) and V refers to the cavity body. The mass sensitivity of our device is determined by the energy percentage of surface A in the total stored mechanical energy of the cavity body. In the region of the red circle in figure 2, the energy percentage of the 5th mode is much larger than that of the 3rd mode, which implies the huge mass sensitivity difference between the two modes. From equation (2), the theoretical mass sensitivities of the two modes are 7.3 and 0.2 Hz ng^{-1}. If mass is selectively loaded here, the 5th mode responds to both mass and temperature changes greatly while the 3rd mode is only sensitive to temperature changes. By monitoring frequency shifts of the two modes simultaneously, temperature interference can be efficiently removed from mass measurement. So this area is selected as the sensing surface. The 3rd and 5th modes need to be excited simultaneously and efficiently with a proper electrode design.

We fabricate the PnC point defect structure by micro electromechanical system (MEMS) technologies. The 380 μm thick Si wafer is first cleaned using sulfuric acid solution and deionized water. After lithography and developing, an Al film about 300 nm thick is deposited by evaporation. The Al film is lifted off in acetone to form the mask for deep-reactive ion etching (D-RIE) (figure 3(a)(i)). Then the wafer is etched by the D-RIE process and the etching depth is 190 μm. By repeating similar procedures on the other side of the wafer, the through holes of PnC are built (figure 3(a)(ii)). A 100 nm molybdenum (Mo) layer is deposited as the ground electrode and the seeding layer of the 1.5 μm thick piezoelectric AlN film, which is deposited by direct current (dc) reactive sputtering (figure 3(a)(iii)). The top Al electrode is then patterned by using the lift-off procedure. Finally, part of the AlN film at the edge is etched by KOH solution to expose the Mo ground electrode (figure 3(a)(iv)). The fabricated

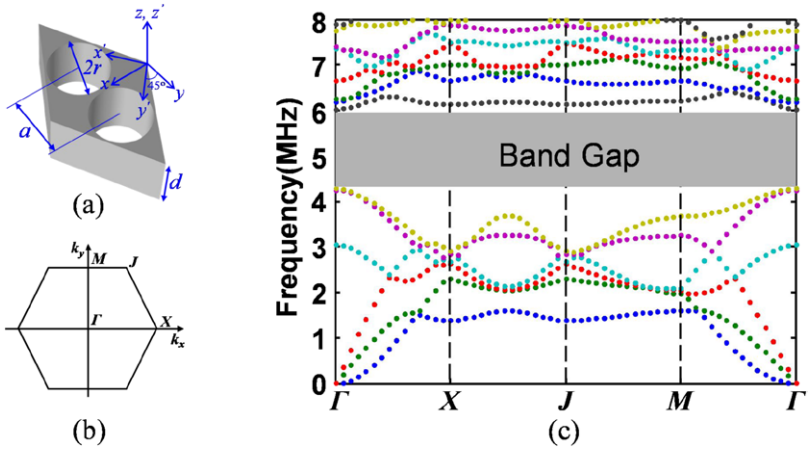

Figure 1. (a) A unit cell of the hexagonal lattice PnC with geometry parameters $a = 380$ μm, $r = 170$ μm and $d = 380$ μm. a, r, and d represent the distance between the two nearest holes, radius of holes, and the slab thickness, respectively. The main axes of the PnC coordinate system xyz are rotated about the z' axis of the Si coordinate system $x'y'z'$ though an angle of 45°. (b) The reduced Brillouin zone of the PnC. (c) The band structure of the PnC. The shaded region represents the complete band gap ranging from 4.3 to 6.0 MHz.

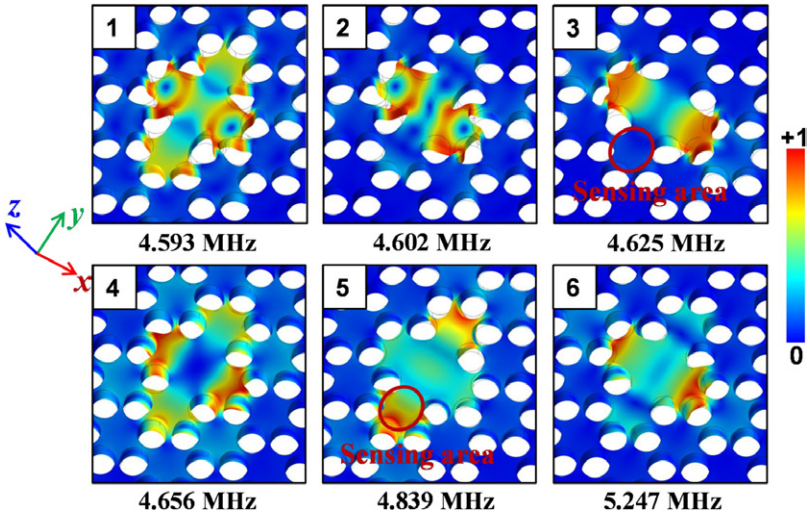

Figure 2. Simulated mode shapes and frequencies. The color bar represents the displacement amplitude in an arbitrary unit. The circled area in the mode shapes of the 3rd and 5th modes is selected as the sensing area. xyz is the PnC coordinate system.

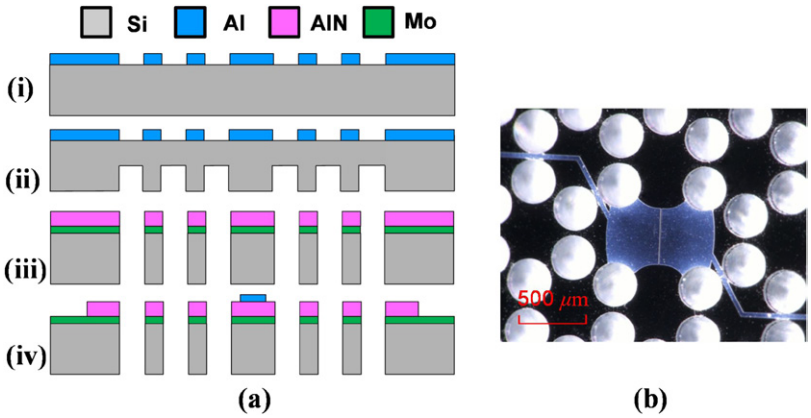

Figure 3. (a) Fabrication process of the PnC resonator: (i) deposition and patterning of Al mask, (ii) two-step etching of Si to build through holes of PnC, (iii) deposition of Mo ground electrode and AlN piezoelectric layer, and (iv) deposition and patterning of top Al electrode and etching of AlN at the edge. (b) Microscope image of the fabricated PnC resonator. The white part is the top Al electrode.

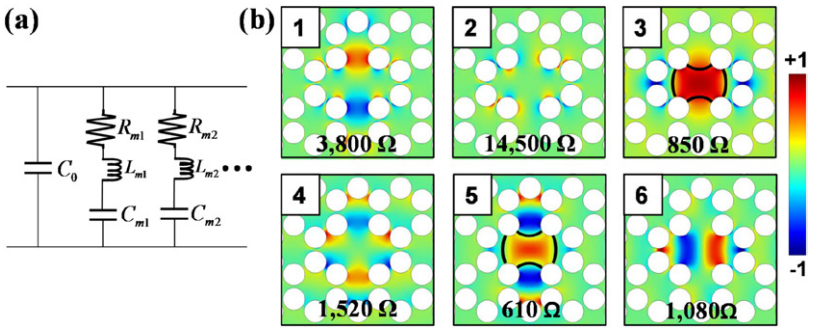

Figure 4. (a) The BVD equivalent circuit model for a resonator with multiple resonant modes; (b) the normal surface charge distributions of all defect modes at maximum deformations and the minimum motional impedances R_m in the case of $Q = 10000$. The color bar denotes the charge density amplitude in an arbitrary unit. The circled area in the charge distribution of the 3rd and 5th modes marks the place to put the common excitation electrode of the two modes.

PnC resonator is shown in figure 3(b) and the white part is the top Al electrode.

3. Method and experiment of mode selection

The BVD equivalent circuit model is widely used to characterize the performance of MEMS resonators. Based on this model, we propose an electrode design method to maximize the displacements of a single defect mode. In figure 4(a), C_0 denotes the parasitic capacitance of the electrode and each R_m–L_m–C_m (motional resistance, inductance and capacitance) branch represents the motional behavior of a specific mode. At the resonance of the mode, the branch is purely resistive and lower motional resistance R_m means a larger current passing through the branch at constant excitation voltage. According to an electrical–mechanical analogy, a larger current corresponds to larger mode displacements. Thus, to selectively excite one mode is to minimize the corresponding R_m. According to the continuity of current, the peak current I_0 through the branch corresponding to the mode can be calculated by integrating the normal surface charge density D_n in the electrode covered region A at maximum displacements, that is

$$I_0 = \omega_s \iint_A D_n \mathrm{d}A, \tag{3}$$

where ω_s is the angular frequency of the mode. The Q factor of the mode is defined as

$$Q = \frac{\omega_s E}{P_d}, \tag{4}$$

where $P_d = I_0^2 R_m/2$ is the time-averaged dissipation power and E refers to the total energy of the resonator. E is constituted by the electromagnetic and mechanical energy in the AlN film (1.5 μm) and the mechanical energy in the Si (380 μm). However, the former part is negligible compared with the latter part because of the thickness contrast. The Q factor of the mode needs to be known or well estimated in advance. Then R_m can be expressed as

$$R_m = \frac{2E}{Q\omega_s} \frac{1}{\left(\iint_A D_n \mathrm{d}A\right)^2}, \tag{5}$$

The distribution of D_n can be estimated through the surface charge D_n^m at maximum deformation in modal analysis and the superscript m refers to modal analysis. In the modal analysis, the top and bottom electrodes are short-circuited to remove the effect of C_0. Because of the linear and quadratic dependence of the charge and energy on deforming displacements, respectively, R_m can be evaluated as

$$R_m = \frac{2E^m}{Q\omega_s} \frac{1}{\left(\iint_A D_n^m \mathrm{d}A\right)^2}, \tag{6}$$

where E^m is the mechanical energy in the Si slab in the modal analysis. To minimize R_m, the absolute of $\iint_A D_n^m \mathrm{d}A$ should be maximum. The cavity comprises two subdomains Ω_+ and Ω_-, representing the areas where signs of the normal surface charge are uniformly positive and uniformly negative, respectively. To maximize the absolute value of $\iint_A D_n^m \mathrm{d}A$, it is easy to see that one should choose either Ω_+ or Ω_- to be the metallized area. The charge distributions of the cavity modes at maximum deformation obtained using the modal analysis are shown in figure 4(b). Given a random Q factor (for example 10^4) for all modes, the corresponding optimum motional resistances according to equation (6) are presented at the same time. It should be noted that with known Q factors, besides predicating the optimum electrode for any single mode, equation (6) can also be used to evaluate the performance of the resonator under any electrode coverage.

To test the validity of the method, according to the charge distribution of the 4th and 5th modes, we design two kinds of one-port devices (electrodes shown in figure 5) to excite them. The FEM simulated conductance results corresponding to the two electrode designs are plotted in figure 5. The independent elastic constants of AlN is $C_{11} = 410$ GPa, $C_{12} = 149$ GPa, $C_{13} = 99$ GPa, $C_{33} = 389$ GPa, $C_{44} = 125$ GPa and the density is 3300 kg m^{-3}. The independent piezoelectric stress constants of AlN are $e_{15} = -0.48$ C m^{-2}, $e_{31} = -0.58$ C m^{-2}, $e_{33} = 1.55$ C m^{-2} and the relative permittivity is 9, taken from COMSOL. The loss factors in simulations are given according to the extracted Q factors by fitting the equivalent circuit (mentioned below). The conductance curves of these two one-port devices are measured by a network analyzer (Agilent 4395a)

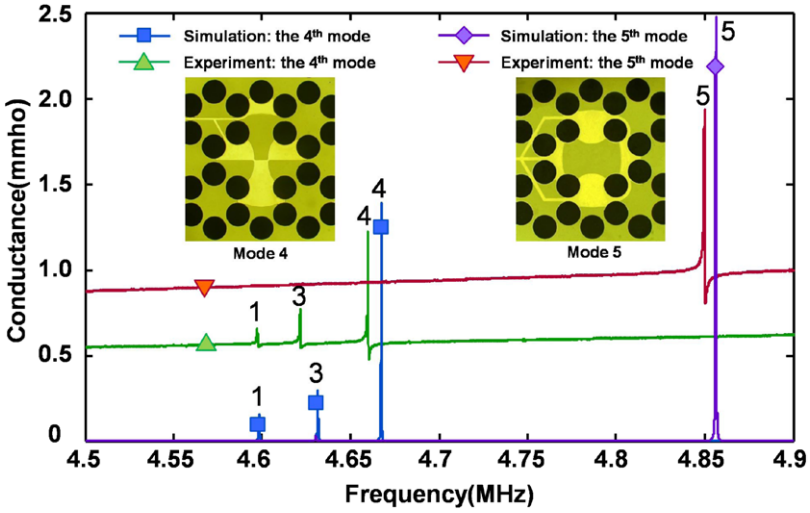

Figure 5. Simulated and experimental conductance curves corresponding to two different electrodes. The excited modes are numbered in agreement with figure 2. Insets: microscope images of electrode layouts for exciting the 4th and 5th modes.

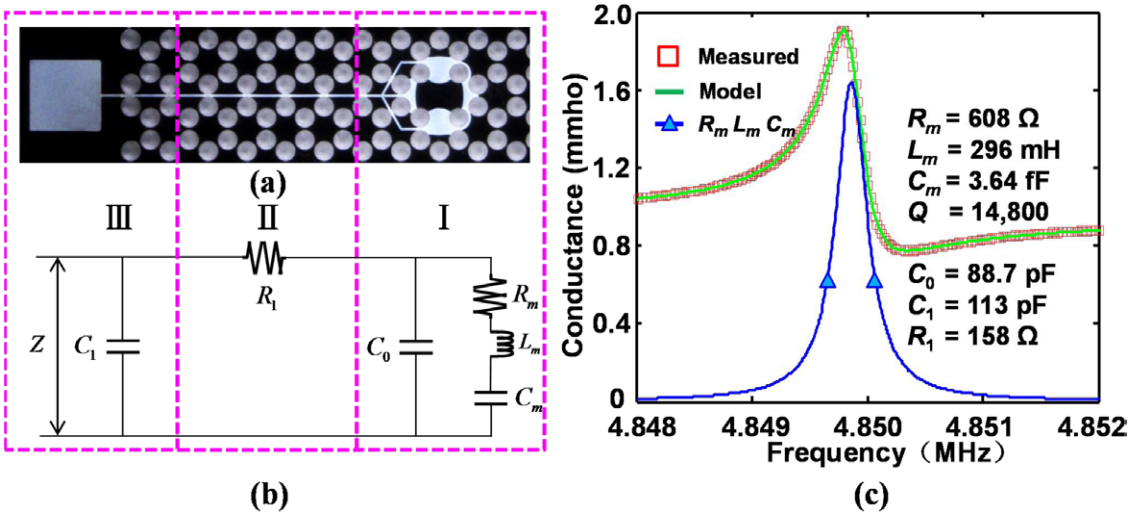

Figure 6. (a) The whole electrode for exciting the 5th mode. Part I is the electrode inside the cavity, part II is the connection wire and part III is the contact pad; (b) the equivalent circuit corresponding to the three parts in (a); (c) the extracted parameters by fitting the model in (b) and the conductance curves of the 5th mode: the measured (red square), the fitted (green line) and plotted by only R_m–L_m–C_m (blue triangle line).

and also shown in figure 5. The frequencies of the resonant peaks are in good agreement with simulations. Therefore, the desired 4th and 5th modes can be selectively excited efficiently. The 5th mode has realized single mode excitation.

Shown in figure 6(a) is the complete electrode layout to excite the 5th mode. The electrode consists of three parts: the cavity electrode, the connection wire and the contact pad. The corresponding equivalent circuit model is plotted in figure 6(b). In part I, the R_m–L_m–C_m branch still represents the motional behavior of the 5th mode, while C_0 accounts for the parasitic capacitance of the cavity electrode. The resistance of the connection wire (part II) and capacitance of the contact pad (part III) are represented by R_1 and C_1. R_1 cannot be neglected because of the long electrical connection between the contact pad and defect electrode. The experimental conductance of the 5th mode is in good agreement with our model (figure 6(c)). This model also explains the upshift of the conductance baseline and the asymmetry of resonant peaks in the experiment (figure 5). The fitted values are listed in the same plot. The extracted Q factors of the 4th and 5th modes are 21 300 and 14 800, respectively, which prove the efficient energy confinement by point defect. The extracted R_m of the two modes are 986 and 608 Ω, which are larger than the calculated 710 and 410 Ω by substituting the fitted Q factors into equation (6). This can be attributed to the imperfection of the deposited AlN film in piezoelectric transduction. The extracted R_m is large compared with typical MEMS piezoelectric resonators like FBARs (film bulk acoustic resonators). The large motional resistance can lead to the impedance mismatch of the devices with 50 Ω transmission lines, resulting in significant insert loss. In this paper, the importance of R_m is not that significant if only a high SNR (signal-to-noise ratio) can be ensured. The blue solid line in figure 6(c) represents the conductance peak of the 5th mode using fitted R_m–L_m–C_m and is sharper

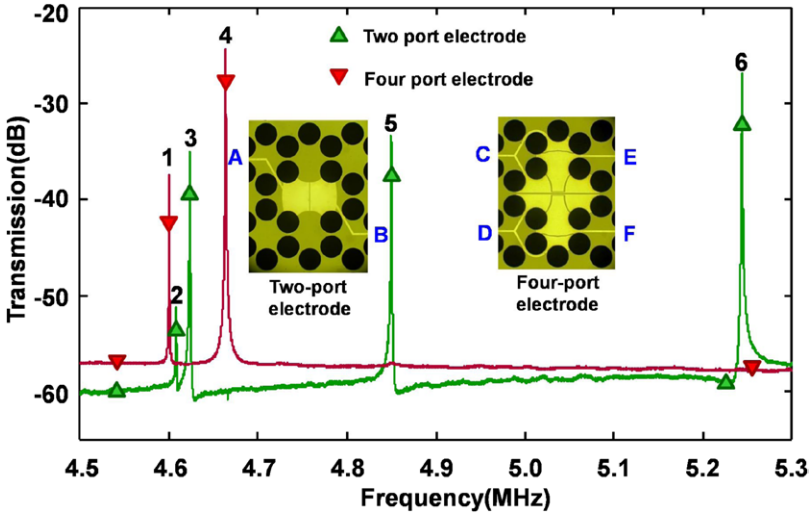

Figure 7. The experimental transmission spectrums of the two-port device (green line) and the four-port device (red line). The excited modes are numbered in agreement with figure 2. Insets: microscope images of the electrodes.

than the measured curve. It is clear that in the impedance (or reflection) measurement of one-port devices, R_1 decreases the sharpness of the resonance peak, which equivalently lowers frequency resolution. In the transmission measurements of multiport devices, the sensing electrodes only penetrate into the R_m–L_m–C_m branch and hardly any signal can be detected when there is no resonance. So the effect of R_1 on the resonant peak sharpness in transmission measurement can be greatly reduced compared with that in the one-port impedance measurement. Multiport devices are expected to be more advantageous over one-port devices in frequency resolution.

To excite the 3rd and 5th modes simultaneously, the electrode should be placed where the absolute value of the charge integral in equation (6) should be large for both modes. The region delimited by the black line in figure 4 is selected because most of the positive charge (78% and 85%) of the two modes gathers here. In the corresponding two-port electrode layout in figure 7, port **A** excites and port **B** measures the vibrations. The transmission spectrum measured by the network analyzer (Agilent 4395a) shows that both modes have strong responses. Furthermore, the 2nd and 6th modes are also detected. The asymmetry resonant peaks (green) in figure 7 denote the existence of capacitive coupling between the electrode plates which is unavoidable because of the narrow cavity. According to the charge distribution of the 4th mode in figure 2(b), we design a four-port electrode, in which ports C and D actuate differentially and ports E and F sense differentially. The transmission peaks (red) become symmetrical. Hence, differential electrodes can greatly suppress capacitive coupling. Thus all modes can be excited in groups by the two kinds of electrode patterns. The measured frequencies and Q factors by 3 dB bandwidth are listed in table 1. The measured mode frequencies agree well with simulation. The Q factors of the 4th and 5th modes, 20 200 and 13 900, generally agree with those extracted by fitting the model in figure 6(a), 21 300 and 14 800. Thus Q degradation though transmission measurements is considerably weaker than that through impedance measurement, proving that transmission measurements perform better in frequency resolution.

Table 1. Experimental frequencies and Q factors.

Mode	1	2	3	4	5	6
F (MHz)	4.600	4.603	4.623	4.664	4.850	5.244
Q	17 200	9220	15 400	20 200	13 900	14 600

4. Temperature compensation experiments

The temperature sensitivities of the 3rd and 5th modes were measured by putting the two-port device in a thermal oven, which was heated to 40 °C and then cooled. The temperature variation was monitored by Pt100. The experiment revealed that temperature sensitivities of the modes are −31.2 and −30.9 ppm°C^{-1}, which agree well with expectation.

The temperature compensation experiment is carried out by loading water droplets containing magnetic beads (diameter 2.8 μm, 15.4 pg each) with a metal ring (inner diameter ~400 μm) to the sensing surface on the Si side of the cavity four times. The droplet volumes are about 20 nl. It takes about 20 s for a droplet to evaporate, which is enough for the loading. If the droplet sizes become smaller, the evaporation problem will become serious and quicker transfer will be needed. The method of depositing solutes using spray nozzles may be adopted [25]. The total mass of the added beads is about 9.3 ng by numbering loaded beads. The frequency shifts of both modes are measured alternately with a sweeping period of 11.2 s by the network analyzer (Agilent 4395a). During each period, 401 frequency points are measured with a total span of 2 KHz. Since the transmission peak shapes are hardly disturbed in the loading intervals, a weighted centroid method is performed to improve the accuracy of the frequency shift measurement. Assuming the transmission peak value is T_m, the frequency points with transmission values in $[T_m - 3, T_m]$ were averaged with their transmission differences to $T_m - 3$ as weights. Shown in figure 8 are the frequency shifts of the 3rd mode (squares) and the 5th mode (diamonds). Once the drop is loaded, the frequency of the 5th mode is seriously distorted due to the liquid damping, as indicated by the shaded areas, while the frequency of the 3rd mode is less

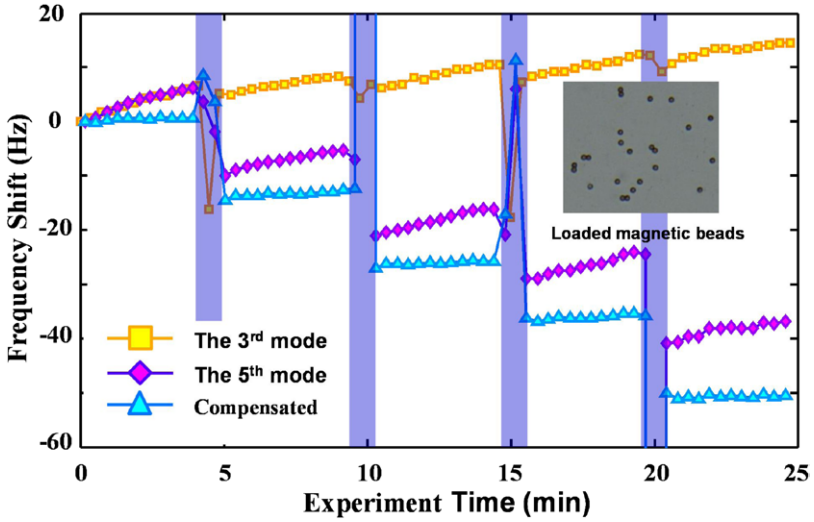

Figure 8. The frequency shifts of the 3rd mode (squares), the 5th mode (diamonds) and the compensated (triangles). Unstable curves in the shaded region represent the evaporation process. Inset: microscope image of the loaded magnetic beads.

affected because of the different energy distributions. During each loading, the frequencies of both modes are rising due to the environmental temperature variation. After each loading, the frequency of the 5th mode decreases significantly, while the 3rd mode is almost immune to this mass loading. By combining the two modes, we can compensate the temperature variation (triangles in figure 8) efficiently and the long-term temperature drift is removed. It should be noted that frequency shifts between two successive loadings are not exactly the same. This may be attributed to the liquid volume fluctuations of each loading. At the end of the experiment, the total frequency shift of the 5th mode with compensation is 50.4 Hz and the estimated mass sensitivity is 5.4 Hz ng^{-1}, which generally agrees with the calculated 7.3 Hz ng^{-1}. We can see that with only the 5th mode, the relative error due to temperature variation is about 27% at the end of the experiment.

5. Conclusions

In summary, we have realized the maximum actuation of a single PnC point defect mode by patterning the electrodes according to the normal surface charge distributions determined by mode deformation. The electrode design method does not consider the responses of other modes and is feasible with the resonators working in a frequency sweeping manner. If combined with optimization methods such as topology optimization [26], the electrode design method is promising for application in cases where responses of unwanted modes need to be effectively suppressed, such as oscillators. We have applied the method to design resonators with different port numbers and proved that multiport devices are advantageous in frequency resolution. A Q factor as high as 21 300 is obtained in air, proving the efficient energy confinement by point defect. Additionally, we have designed a mass sensor based on a two-port resonator and two defect modes with different mass sensitivities are selectively excited to compensate temperature changes. The experiment reveals that temperature interference is effectively removed and the mass sensitivity is 5.4 Hz ng^{-1}. The sensitivity can be greatly enhanced by downsizing the device. Considering the device fragility and fabrication limitations, devices with a thickness of 10–20 μm can be fabricated on SOI (silicon-on-insulator) wafers. Thus devices with resonant frequencies of about 100 MHz can be expected. We believe that mode selection or sensing mechanism can promote the applications of high Q, mode selected PnC cavities in signal processing and sensing.

Acknowledgments

This work was supported by the Instrument Developing Project of the Chinese Academy of Sciences (YZ201353), the National Natural Science Foundation of China (Nos 51205381, 11572318, 61271139, 51505456), the Jilin Province Development and Reform Commission (2015Y028) and the Science and Technology Development Program of Jilin Province (No. 20130522185JH, No 20140101057JC, No 20150520110JH). The authors wish to thank the staff at Tianjin University ROFS Microsystem for their help in the fabrication of AlN film.

References

[1] Kushwaha M S, Halevi P, Dobrzynski L and Djafari-Rouhani B 1993 Acoustic band structure of periodic elastic composites *Phys. Rev. Lett.* **71** 2022
[2] Liu Z, Zhang X, Mao Y, Zhu Y, Yang Z, Chan C and Sheng P 2000 Locally resonant sonic materials *Science* **289** 1734–6
[3] Yang S, Page J, Liu Z, Cowan M, Chan C and Sheng P 2004 Focusing of sound in a 3D phononic crystal *Phys. Rev. Lett.* **93** 024301
[4] Sukhovich A, Merheb B, Muralidharan K, Vasseur J, Pennec Y, Deymier P and Page J 2009 Experimental and theoretical evidence for subwavelength imaging in phononic crystals *Phys. Rev. Lett.* **102** 154301

[5] Hopkins P E, Reinke C M, Su M F, Olsson R H III, Shaner E A, Leseman Z C, Serrano J R, Phinney L M and El-Kady I 2010 Reduction in the thermal conductivity of single crystalline silicon by phononic crystal patterning *Nano. Lett.* **11** 107–12

[6] Khelif A, Choujaa A, Benchabane S, Djafari-Rouhani B and Laude V 2004 Guiding and bending of acoustic waves in highly confined phononic crystal waveguides *Appl. Phys. Lett.* **84** 4400

[7] Mohammadi S, Eftekhar A A, Hunt W D and Adibi A 2009 High-*Q* micromechanical resonators in a 2D phononic crystal slab *Appl. Phys. Lett.* **94** 051906

[8] Wang N, Hsiao F-L, Tsai J M, Palaniapan M, Kwong D-L and Lee C 2013 Numerical and experimental study on silicon microresonators based on phononic crystal slabs with reduced central-hole radii *J. Micromech. Microeng.* **23** 065030

[9] Li F, Liu J and Wu Y 2011 The investigation of point defect modes of phononic crystal for high *Q* resonance *J. Appl. Phys.* **109** 124907

[10] Lucklum R, Ke M and Zubtsov M 2012 2D phononic crystal sensor based on a cavity mode *Sens. Actuators* B **171–172** 271–7

[11] Amoudache S, Pennec Y, Djafari Rouhani B, Khater A, Lucklum R and Tigrine R 2014 Simultaneous sensing of light and sound velocities of fluids in a 2D phoXonic crystal with defects *J. Appl. Phys.* **115** 134503

[12] Li F, Wu Y, Manceau J-F o and Bastien F o 2008 Temperature compensation of lamb wave sensor by combined antisymmetric mode and symmetric mode *Appl. Phys. Lett.* **92** 074101

[13] Mu X, Kropelnicki P, Wang Y, Randles A B, Chai K T C, Cai H and Gu Y D 2014 Dual mode acoustic wave sensor for precise pressure reading *Appl. Phys. Lett.* **105** 113507

[14] Dohn S, Svendsen W, Boisen A and Hansen O 2007 Mass and position determination of attached particles on cantilever based mass sensors *Rev. Sci. Instrum.* **78** 103303

[15] Wang T, Mu X, Kropelnicki P, Randles A B and Lee C 2014 Viscosity and density decoupling method using a higher order Lamb wave sensor *J. Micromech. Microeng.* **24** 075002

[16] Melamud R, Chandorkar S A, Kim B, Lee H K, Salvia J C, Bahl G, Hopcroft M and Kenny T W 2009 Temperature-insensitive composite micromechanical resonators *J. Microelectromech. Syst.* **18** 1409–19

[17] Mohammadi S, Eftekhar A A, Pourabolghasem R and Adibi A 2011 Simultaneous high-*Q* confinement and selective direct piezoelectric excitation of flexural and extensional lateral vibrations in a silicon phononic crystal slab resonator *Sensors Actuators* A **167** 524–30

[18] Lee C-K and Moon F C 1990 Modal sensors/actuators *Trans. ASME* **57** 434–41

[19] Sanchez-Rojas J L, Hernando J, Donoso A, Bellido J C, Manzaneque T, Ababneh A, Seidel H and Schmid U 2010 Modal optimization and filtering in piezoelectric microplate resonators *J. Micromech. Microeng.* **20** 055027

[20] Ruiz-Díez V, Manzaneque T, Hernando-García J, Ababneh A, Kucera M, Schmid U, Seidel H and Sánchez-Rojas J L 2013 Design and characterization of AlN-based in-plane microplate resonators *J. Micromech. Microeng.* **23** 074003

[21] Butterworth S 1914 On electrically-maintained vibrations *Proc. Phys. Soc. Lond.* **27** 410

[22] Van Dyke K 1928 The piezo-electric resonator and its equivalent network *Proc. IRE* **16** 742–64

[23] Mohammadi S, Eftekhar A A, Khelif A, Moubchir H, Westafer R, Hunt W D and Adibi A 2007 Complete phononic bandgaps and bandgap maps in 2D silicon phononic crystal plates *Electron. Lett.* **43** 898

[24] Auld B A 1990 *Acoustic Fields and Waves in Solids* (Malabar, FL: Krieger) p 318

[25] Müller T, White D and Knowles T 2014 Dry-mass sensing for microfluidics *Appl. Phys. Lett.* **105** 214101

[26] Donoso A and Bellido J C 2008 Systematic design of distributed piezoelectric modal sensors/actuators for rectangular plates by optimizing the polarization profile *Struct. Multidiscip. Optim.* **38** 347–56